Nanoscale Advances

ROYAL SOCIETY OF CHEMISTRY

PAPER

View Article Online
View Journal | View Issue

Cite this: *Nanoscale Adv.*, 2022, **4**, 1599

The electronic structure of the metal–organic interface of isolated ligand coated gold nanoparticles†

Robin Schürmann, *[a] Evgenii Titov, [a] Kenny Ebel,[a] Sergio Kogikoski, Jr, [a] Amr Mostafa,[a] Peter Saalfrank, [a] Aleksandar R. Milosavljević[b] and Ilko Bald *[a]

Light induced electron transfer reactions of molecules on the surface of noble metal nanoparticles (NPs) depend significantly on the electronic properties of the metal–organic interface. Hybridized metal–molecule states and dipoles at the interface alter the work function and facilitate or hinder electron transfer between the NPs and ligand. X-ray photoelectron spectroscopy (XPS) measurements of isolated AuNPs coated with thiolated ligands in a vacuum have been performed as a function of photon energy, and the depth dependent information of the metal–organic interface has been obtained. The role of surface dipoles in the XPS measurements of isolated ligand coated NPs is discussed and the binding energy of the Au 4f states is shifted by around 0.8 eV in the outer atomic layers of 4-nitrothiophenol coated AuNPs, facilitating electron transport towards the molecules. Moreover, the influence of the interface dipole depends significantly on the adsorbed ligand molecules. The present study paves the way towards the engineering of the electronic properties of the nanoparticle surface, which is of utmost importance for the application of plasmonic nanoparticles in the fields of heterogeneous catalysis and solar energy conversion.

Received 11th October 2021
Accepted 31st January 2022

DOI: 10.1039/d1na00737h

rsc.li/nanoscale-advances

Introduction

The electron transfer reactions of illuminated noble metal nanoparticles (NPs) play a significant role in the conversion of solar light to chemical energy.[1,2] These reactions are mediated by the localized surface plasmon resonances (LSPRs) of the NPs, which are collective oscillations of the conduction band electrons that are excited by incident light.[3–5] In a non-radiative decay process of the LSPR, electron–hole pairs are formed, which can be transferred directly or indirectly to molecules adsorbed on the NP surface and trigger reactions therein.[6–11] The reaction of 4-nitrothiophenol (NTP) to 4′,4-dimercaptoazobenzene (DMAB) on metal surfaces is a show-case reaction for plasmon mediated chemistry.[12–24] Even though the parameters determining the reaction are still under debate, it is assumed to be triggered by an electron transfer from the NPs to the adsorbed molecules forming a stable anion.[12,13,15,16,18,20,25] In addition to the electron transfer also a hole transfer from the NPs to the adsorbed molecules has a significant role in the dimerization of NTP.[26] The transfer probability depends significantly on the electronic properties like the density of initial and final states and work function, which are significantly influenced by the metal–organic interface.[4,13,27] By tuning the properties of the metal–organic interface, the electron or hole transfer can be optimized. Self-assembled molecular monolayers of thiolated molecules like NTP significantly alter the properties of Au substrates, namely work function[28,29] and electronic states,[30] when the Fermi levels of the molecular layer and NPs are pinned[31] due to the formation of hybridized molecular-metallic states.[32] The work function of a metal can be significantly altered by molecular dipole moments, whereas the resulting work function of the system depends mainly on the adsorbed molecules.[33–35] Moreover, by tailoring the molecular dipoles the electronic states at the metal–organic interface can be tuned.[33,36] The properties of the NP–ligand interface can be either affected by the functional groups of the molecules or by their packing density and alignment.[34] Recently, it has been demonstrated by comparing the plasmon mediated formation of diazo bonds from NTP and 4-nitrobenzylmercaptan (NBM) that the reaction kinetics are significantly influenced by the molecular geometry.[37] The in-depth knowledge of the electronic properties at the molecule–NP interface allows efficient tuning of the kinetics of plasmon mediated electron transfer reactions.[38] Therefore, the following needs to be understood:

- How are the electronic states on the NP surface altered by the adsorption of ligand molecules?
- What is the range of the effects that alter the electronic properties at the interface?

[a]*University of Potsdam, Institute of Chemistry, 14476 Potsdam, Germany. E-mail: robin.schuermann@uni-potsdam.de; ilko.bald@uni-potsdam.de*

[b]*Synchrotron SOLEIL, 91192 GIF-sur-YVETTE CEDEX, France*

† Electronic supplementary information (ESI) available. See DOI: 10.1039/d1na00737h

• How are the electronic states of the adsorbed molecules affected by the adsorption on the NPs?

Within this work we study the electronic properties, namely work function and core level states, by XPS of isolated NTP coated AuNPs and elucidate the role of surface dipoles by comparison with NBM. By tuning the inelastic mean free path (IMFP) of the generated photoelectrons, depth dependent information is obtained.

Results and discussion

In the present experiments a focused beam of ligand coated AuNPs has been generated and transferred into a vacuum, where it is crossed with the tunable soft X-ray beam of the PLEIADES beamline at the Synchrotron SOLEIL to perform X-ray photoelectron spectroscopy (XPS) measurements (see Fig. 1(a)). In this way, both the X-ray induced photodamage to the studied NPs and the effects from a substrate are prevented.

In a typical solid state XPS experiment, the sample and the detector are grounded; hence the reference energy for the binding energy (BE) is the Fermi energy, which is calibrated with well-accepted binding energies, *e.g.* the C 1s state of adventitious carbon or the Au $4f_{7/2}$ state of bulk gold.[39,40] However, in the present experiment the AuNPs are isolated in a vacuum and the detector and sample are decoupled, which leads to the consequence that the Fermi energy of the sample and detector might differ.[41] Therefore, the ionization energies of dilute Ar[42] gas have been used for the calibration of the kinetic energy (KE) of the photoelectrons, and hence, the vacuum energy of Ar is the reference of the BE (see Fig. S3†). In Fig. 1(c) an energy diagram of the XPS measurements of isolated NPs is presented, showing that the vacuum energy of Ar gas and the vacuum energy at the surface of the NPs might differ due to the action of the surface dipoles of the NP sample.[43,44] In consequence, the energy difference between the BEs determined in the present experiment (*i.e.* with respect to the vacuum level) and the BEs determined in solid state XPS experiments (*i.e.* with respect to the Fermi level) corresponds to the work function φ of the NP system reduced by the dipole energy of the surface. It has to be noted that, in contrast to ambient pressure XPS measurements,[45] an impact of the surface dipoles of the sample on the vacuum energy of the Ar atoms can be neglected due to the small size and dilute concentration of the NPs in a vacuum (see Fig. S4† for details).

Depth dependent measurements of isolated AuNPs

XPS is a very surface sensitive technique, which allows the determination of the composition and position of electronic states in a material, as the inelastic mean free path (IMFP) of the photoelectrons is limited.[46–48] The effective sampling depth in XPS is three times the IMFP of the sample, and therefore, only those photoelectrons that are generated in the outer layers of the AuNPs can escape the particle and reach the detector, even though they are produced through the entire NPs. In XPS measurements, the KE of the photoelectrons originating from an atomic shell with a certain BE depends linearly on the photon energy (PE):

$$\mathrm{KE} = \mathrm{PE} - \mathrm{BE}. \quad (1)$$

The IMFP λ of electrons, which gives the average path length an electron can move in a solid without an inelastic scattering event, depends significantly on their KE:[49]

$$\lambda = \frac{A}{\mathrm{KE}^2} + B\sqrt{\mathrm{KE}}. \quad (2)$$

Hence, the IMFP of the generated photoelectrons can be tuned by the PE and the depth dependent information of the NP/ligand interface can be obtained. XPS measurements of AuNPs with an average diameter of 10 nm coated with NTP have been performed as a function of the PE to vary the KE and in consequence the IMFP of the photoelectrons. In Fig. 2(a) the Au 4f spectra of the NTP coated AuNPs are presented, and have

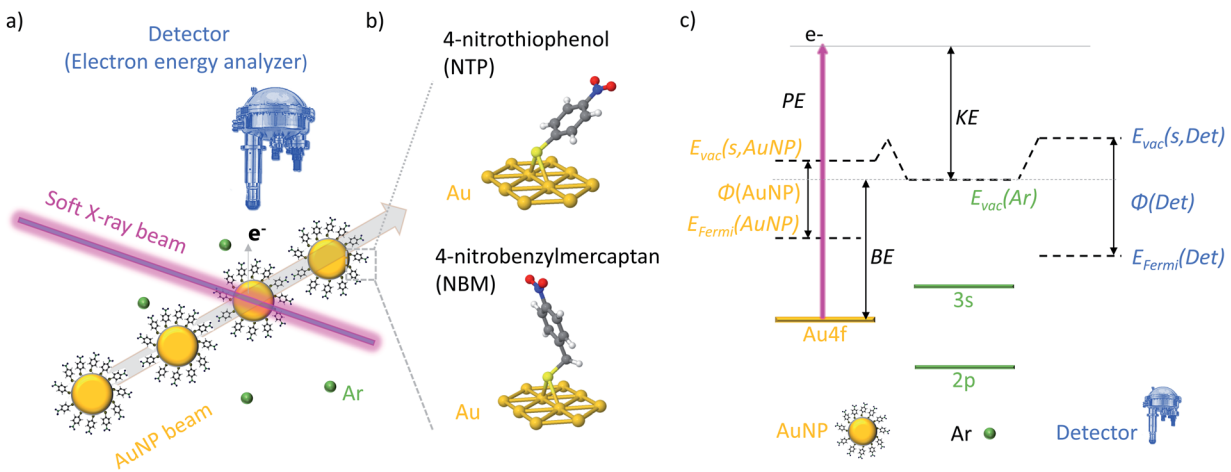

Fig. 1 (a) Scheme of the crossed NP-beam X-ray-beam setup at the PLEIADES beamline. (b) Schematic representation of the two ligand molecules NTP and NBM, which are bound to the AuNP surface. (c) Energy diagram of the XPS measurements and KE calibration of isolated AuNPs.

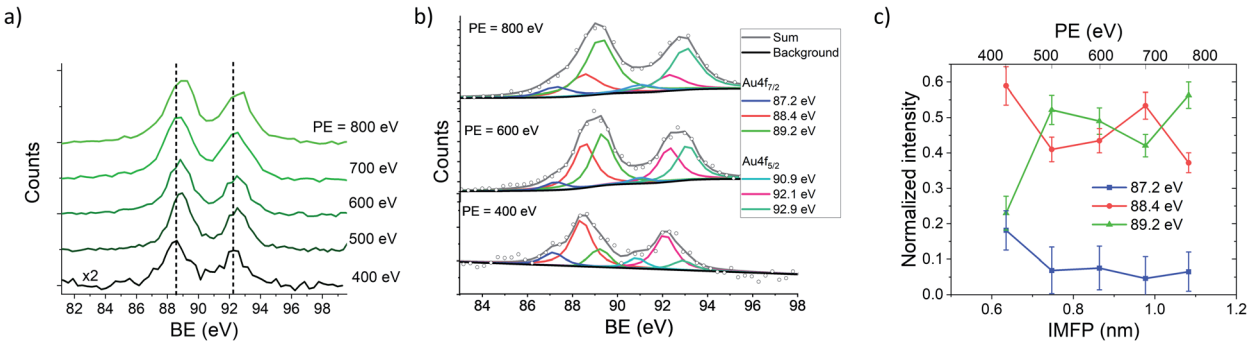

Fig. 2 (a) Au 4f spectra of NTP capped AuNPs recorded at PEs between 400 eV and 800 eV. Dashed lines at 88.5 eV and 92.2 eV represent the center of the peak maxima of the lower spectrum recorded at PE = 400 eV. (b) Au 4f spectra recorded at a PE of 400 eV (ΔPE = 892 meV and ΔKE = 625 meV), 600 eV (ΔPE = 1003 meV and ΔKE = 1250 meV) and 800 eV (ΔPE = 1273 meV and ΔKE = 1250 meV) fitted with 3 components at 88.4 eV, 87.2 eV and 89.2 eV for the Au $4f_{7/2}$ component and the respective Au $4f_{5/2}$ with an intensity of 0.75 of the Au $4f_{7/2}$ signals and a separation of 3.7 eV. The components are fitted with a Voigt function with a Lorentzian to Gaussian ratio of 80 : 20. (c) Intensities of the Au $4f_{7/2}$ components as a function of the IMFP, and the respective PEs are given in the scale above.

been recorded at PEs between 400 eV and 800 eV, wherein special care was taken for a precise calibration of the KE of the photoelectrons at the different PEs to avoid possible effects of the PE peak position (see the Methods part for details). In solid state XPS, the Au 4f signal of bulk Au consists of two components (Au $4f_{7/2}$ and Au $4f_{5/2}$) located at 84.0 eV and 87.7 eV with respect to the Fermi level with a fixed ratio of 4 : 3 due to the spin–orbit coupling.[50] Hence, the KE of the photoelectrons varies between approximately 310 eV to 710 eV, assuming a work function of the AuNPs of around 5 eV. In this case, the IMFP is varied from approximately 0.6 nm to 1.1 nm (ref. 51–53) and in consequence, only the outmost atomic layers of the ligand coated AuNPs are probed in this energy range. Fig. 2 shows that with increasing PE, the maximum of the Au 4f signal shifts from 88.5 eV at PE = 400 eV and reaches 88.9 eV at PE = 800 eV, which indicates a lower BE of the Au atoms at or close to the surface compared to those in the bulk. The Au 4f spectrum recorded at a photon energy of 400 eV reveals three components of the Au $4f_{7/2}$ peak, wherein the most intense is centered at 88.4 eV and two shoulders at 87.2 eV and 89.2 eV respectively (see Fig. 2(b)). For the fitting of the peaks the energy resolution of the photoelectrons has been used as the peak width, which has been validated by the FWHM of the Ar 2p and Ar 3s spectra recorded under the same conditions. Typically on a plane Au(111) surface, three Au species would be expected, namely bulk Au atoms, "free" surface Au atoms and surface Au atoms involved in Au–S bonding.[54–57] The 89.2 eV signal shows a shift of 5.2 eV compared to the Au^0 signal in the solid state located at 84.0 eV, which agrees well with the work function of bulk gold.[58,59] Hence, it is concluded that the 89.2 eV signal originates from the Au atoms inside the AuNPs, where the electronic environment is comparable to that of bulk gold. The signals at 88.4 eV and 87.2 eV are assigned to surface Au atoms, which represent Au(111) facets and further Au species originating from edges or other crystalline facets present on an AuNP surface. The lower binding energy compared to bulk gold might be caused by several, possibly superimposed effects that are shortly explained in the following:

(i) On the one hand, the Au 4f states at a clean Au surface are typically shifted by 0.4 eV to lower BE compared to bulk gold due to a redistribution of the atomic-like valence-band states at the surface, since the coordination number of the surface atoms is lower, which affects the core level states as well.[60,61] Hence, for AuNPs this effect is likely to be even more pronounced than for flat gold surfaces.[62]

(ii) Moreover, surface dipoles caused by ligand molecules at the metal–organic interface can significantly alter the work function and the vacuum energy of coated gold surfaces.[63] Since the Au 4f core level states are localized at the individual gold atoms their BE follows the dipole induced change of the *z*-component of the dipole.[64] The *z*-component of the dipole moment of a complex of NTP coupled to the (111) surface of a cluster of 30 Au atoms has been calculated by density functional theory (DFT) with the B3LYP functional and determined to be −2.88 Debye.

(iii) In addition, also an electron transfer from the metal to the molecule affects the work function, which has been described elsewhere in more detail for the present system.[37]

(iv) A fourth effect is a possible shift of the Au 4f signals due to the different chemical environment of the gold sulfur bond. The shift for NTP coupled to a single Au atom compared to pure Au has been calculated by DFT to be 1.3 eV to higher BE, which is in good agreement with previously reported values for Au–S[65] and other hybridized Au species.[55] For larger Au complexes, the calculated shift of the Au 4f orbitals decreases to 0.9 eV for Au_2 and 0.4 eV for Au_{10}, indicating a minor influence of the chemical shift for larger Au complexes with attached molecules (see Table S1† for details). Moreover, the Au $4f_{7/2}$ signal of species with higher BEs would be overlapped by the 5/2 signal and the 5/2 component would be overlapped by the Lorentzian tail of the higher BE species in a region, which is significantly impacted by the correction of the Shirley type background.

It needs to be mentioned that these four effects act in different directions and raise or lower the BE of the Au 4f states, and consequently, the resulting BE is determined by their superposition. In Fig. 2(b), the decomposition of the peaks

contributing to the Au 4f signal is presented, revealing a predominant contribution of the 88.4 eV signal to the Au $4f_{7/2}$ spectrum recorded at 400 eV, whereas with increasing PE the contribution of the 88.4 eV signal decreases, and the 89.2 eV signal increases. The relative intensities of the Au $4f_{7/2}$ peaks are plotted against the IMFP in Fig. 2(c). The decrease of the 87.2 eV and 88.4 eV signals with an increasing IMFP supports the assignment of these signals to Au atoms located at or close to the surface of the AuNPs, whereas the increase of the 89.2 eV signal with the IMFP confirms that this signal originates from the inner atoms of the AuNPs.

Calculation of the Au shell thickness

The thickness of the Au shell at the interface, where the Au 4f states vary from the bulk gold signal, can be determined from the signal intensities of the different contributions of the Au 4f states. In general, in a substrate covered with a layer of thickness d, the signal intensity I of the underlying substrate is given by:

$$I = I_0\, e^{-d/\lambda}, \quad (3)$$

where I_0 is the unattenuated signal intensity and λ is the IMFP of the photoelectrons in the covering layer. Thus, the thickness d can be calculated from the ratio of the different signal contributions. In the following, the relative intensities of the signals have been calculated for spherical AuNPs. A core–shell–shell structure of the ligand coated AuNPs (10 nm diameter) has been assumed and is sketched in Fig. 3(a). The core consists of Au^0 with the work function of bulk gold, the inner shell consists of Au with altered electronic properties and the outer shell is the organic NTP layer. However, since the NTP layer is attenuating the signal from the Au core and the Au shell by the same factor, only relative and not absolute intensities will be discussed in the following.

To calculate the relative intensities of the XPS signals, it has been assumed that the intensity of the X-ray beam passes through the AuNPs without attenuation, and only non-scattered photoelectrons emitted at a 90° angle have been taken into account. In an infinitesimal small slice, the AuNPs can be considered as a plane layer structure (see Fig. 3(a)), where the relative intensities can be calculated by assuming an exponential signal attenuation of the upper layers shown in eqn (3). By integration of the slices over the whole nanoparticle in cylindrical coordinates, the intensity of the signal originating from the core of the AuNP I_{core} and the signal originating from the Au shell I_{shell} can be obtained by:

$$I_{shell} = 2\pi \int_0^{r_{AuNP}} r \left(1 - e^{-\frac{z_{shell}(r)-z_{core}(r)}{\lambda}} + e^{-\frac{z_{shell}(r)+z_{core}(r)}{\lambda}} - e^{-\frac{2z_{shell}(r)}{\lambda}}\right) dr \quad (4)$$

and

$$I_{core} = 2\pi \int_0^{r_{AuNP}} r \left(e^{-\frac{z_{shell}(r)-z_{core}(r)}{\lambda}} - e^{-\frac{z_{shell}(r)+z_{core}(r)}{\lambda}}\right) dr \quad (5)$$

with $z_{core}(r) = \sqrt{(r_{AuNP} - d_{shell})^2 - r^2}$ and $z_{shell}(r) = \sqrt{r_{AuNP}^2 - r^2}$ (see derivation in ESI, below Fig. S5†). The IMFP λ of the photoelectrons in gold at different KEs has been used from the NIST electron inelastic mean free path database (Version 1.2.) based on the values for gold reported by Powell and Jablonski.[51,53] The contributions I_{shell} and I_{core} to the Au 4f signal have been calculated for different layer thicknesses between 0.2 nm and 1 nm for the IMFP occurring in the XPS measurements of the Au 4f states presented in Fig. 2. In Fig. 3(b) an exemplary plot of normalized I_{core} and I_{shell} *versus* the layer thickness d_{shell} is presented, for an IMFP of 0.86 nm at PE = 600 eV. The plots for the PE of 400 eV, 500 eV, 700 eV and 800 eV are shown in Fig. S6.† The calculated intensities have been fitted with exponential functions to allow an assignment of intensity ratios to Au shell thicknesses at a given IMFP λ. To determine the Au shell thicknesses for the experimental data, the signal intensity of the 89.2 eV Au 4f component determined from the XPS measurements has been used as I_{core} and the sum of the 88.4 eV and 87.2 eV signals as I_{shell}. From the Au 4f spectra presented in Fig. 2(a), the Au shell thickness has been

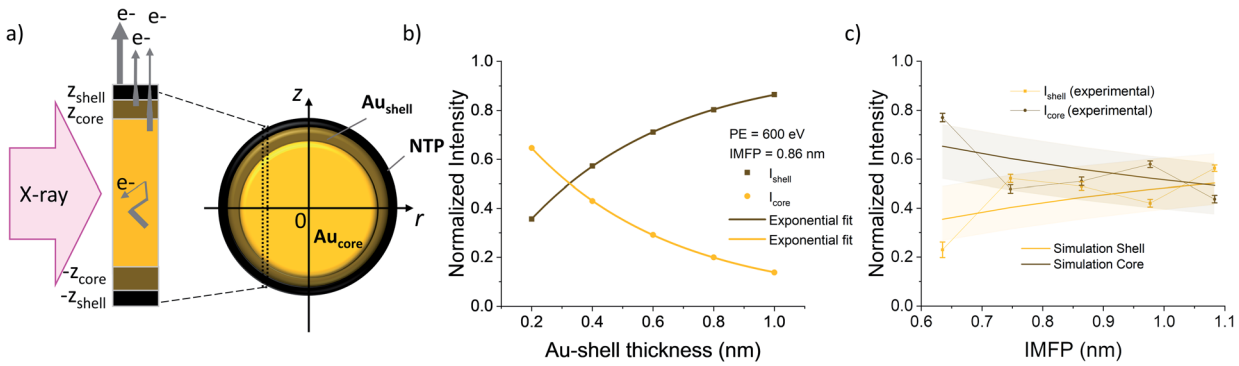

Fig. 3 (a) Sketch of an AuNP with NTP ligands with a cross section of the layers. Arrow thickness on the left side indicates the electron escape probability. (b) Calculated relative intensities originating from the core (gold) and shell (brown) of the AuNPs as a function of the shell thickness fitted with exponential functions. (c) Plot of the relative intensities of the peaks fitted in the Au 4f spectra as a function of the IMFP together with the simulated values for a shell thickness of 0.38 nm. Colored background shows the error interval of the simulated values. The error bars of the experimental values are given by the square root of the absolute peak intensities.

determined using the calculated exponential intensity *vs.* Au shell thickness plots (see Fig. 3(b) and S6†). The Au shell thickness with altered electronic properties at the surface of the NTP coated AuNPs is consequently given by $d_{shell} = 0.38 \pm 0.12$ nm, where the error is given by the standard deviation of the values for d_{shell} for different PEs. In Fig. 3(c), the intensities I_{core} and I_{shell} at different IMFPs for a 10 nm AuNP with an Au shell thickness of 0.38 nm are plotted together with the measured signal intensities of the 89.2 eV, 88.4 eV and 87.2 eV signals, revealing good agreement of the experimental values with applied theoretical model results. As the thickness of the layer with altered Au 4f states is only about 3.8 Å, which corresponds to the first atomic layer of the AuNPs, it can be concluded that the adsorption of ligand molecules impacts electronic properties at the metal–organic interface within a very short range.

Role of ligand molecules

In order to elucidate the influence of the ligands on the XPS signals, we have compared NTP with NBM capped AuNPs. In Fig. 4(a) the Au 4f spectra of NTP and NBM coated AuNPs are presented, which have been recorded at a PE of 400 eV. The IMFP of the photoelectrons is 0.64 nm, and thus the measurements mainly probe the topmost layers of the AuNPs. The center of the Au $4f_{7/2}$ signal of the NBM coated AuNPs is located at 89.1 eV, which is shifted by (0.6 ± 0.2) eV compared to NTP coated AuNPs and indicates a lower work function at the interface. Even though the center of the Au 4f signal is not directly reflecting the states at the surface and is partly overlapped with the bulk signal, the strong contribution of the surface signal clearly indicates a significant shift of these states. The differences of the Au 4f states for the two ligand molecules can be explained by a different dipole moment induced by the ligand molecules. Using DFT the *z*-component of the dipole moment had been calculated for the complex of a molecule bound to an Au_{30} cluster giving −2.88 Debye for the NTP–Au_{30}- and −3.44 Debye for NBM–Au_{30}-complex. This would lead to a shift of the Au 4f states to higher BEs for NBM compared to NTP. The direct calculations of the Au 4f orbitals by DFT reveal a shift of the Au 4f signal of the gold complex of 0.357 eV for NTP–Au_{10} and 0.321 eV for NBM–Au_{10} (see Table S1†). Therefore, the shift of the Au 4f states caused by the different chemical environment of the molecular-metal bonds can be neglected compared to the shifts of the near surface vacuum level by molecular dipoles. Besides the surface dipoles, the differences of the work function can be explained by different packing densities of the molecules, since the adsorption of the molecules can be significantly influenced by the additional carbon linker. Moreover, the packing density can influence the

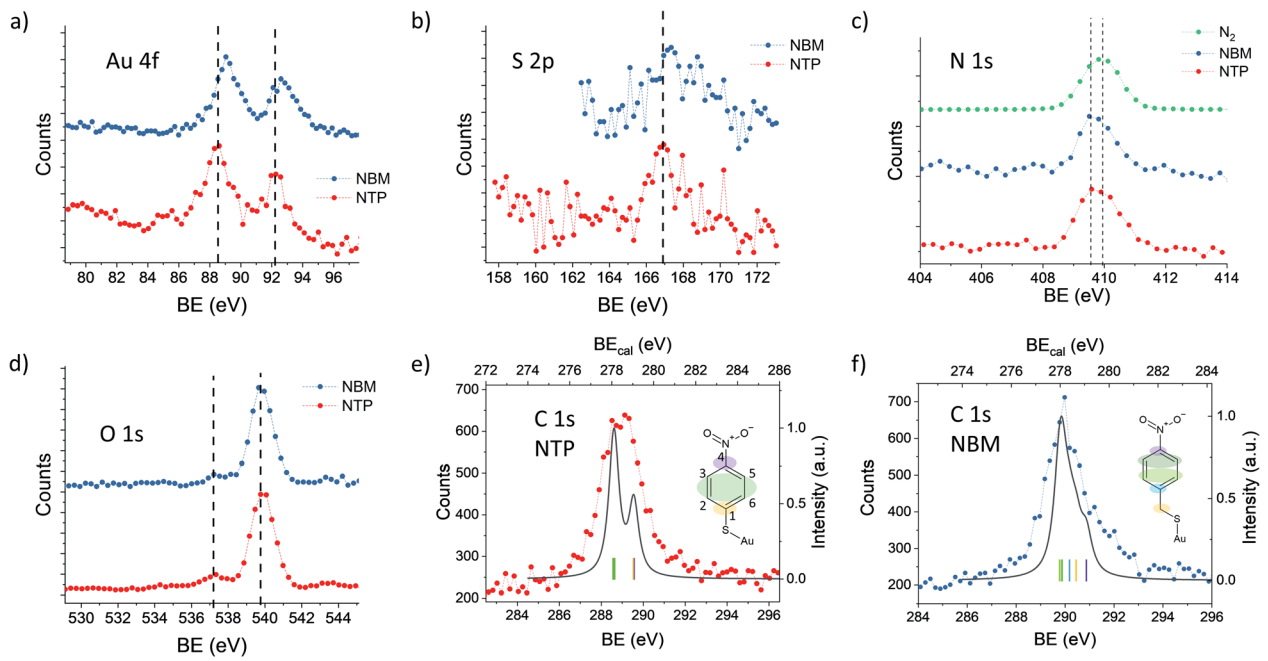

Fig. 4 High resolution XPS spectra of NTP (red) and NBM (blue) coated AuNPs. (a), (c) and (d) have been recorded with Ar carrier gas and (b), (e) and (f) have been recorded with N_2 as the carrier gas to avoid overlap with Ar satellite states. (a) Au 4f spectra recorded at PE = 400 eV (ΔPE = 892 meV and ΔKE = 625 meV) with Ar carrier gas. The dashed line marks the center of the NTP signal to visualize the shift. (b) S 2p spectra recorded at PE = 395 eV (ΔPE = 660 meV and ΔKE = 625 meV). (c) N 1s spectra recorded at PE = 650 eV (ΔPE = 1138 meV and ΔKE = 1250 meV). N 1s of N_2 gas (green) recorded under the same experimental conditions to determine the possible contributions of residual gas molecules. The dashed line marks the maximum of the NBM and of the N_2 signal. (d) O 1s states recorded at PE = 650 eV (ΔPE = 1138 meV and ΔKE = 1250 meV). Dashed lines mark the contribution from the coated AuNPs (left) and of the gas phase water (right). (e) High resolution C 1s spectrum of NTP capped AuNPs recorded at PE = 395 eV (ΔPE = 660 meV and ΔKE = 625 meV) plotted together with the C 1s spectrum of NTP on an Au_{30} cluster obtained by DFT using the same energy resolution. Colored areas on the NTP molecule sketch indicate the origin of the individual signals. (f) C 1s spectrum of NBM capped AuNPs recorded under the same conditions as (e).

alignment of the molecules and consequently affect the *z*-component of the surface dipole.[34] The S 2p spectra shown in Fig. 4(b) reveal a maximum of S $2p_{3/2}$ of 166.9 eV for AuNPs capped with NTP and 167.3 eV capped with NBM. This corresponds to a difference of (0.4 ± 0.2) eV for the NTP capped AuNPs compared to NBM, which is in agreement with the shift of the Au 4f states.

The Au 4f and S 2p spectra reflect the metal–organic interface, whereas the O 1s and N 1s signals originate from the nitro group, which is separated from the gold surface by the benzene ring. In Fig. 4(c), the N 1s spectra of NTP and NBM capped AuNPs are presented together with a spectrum recorded in the same energy range in the absence of AuNPs, when N_2 is introduced into the chamber. The center of the N 1s peak of gaseous N_2 is located at 409.9 eV, whereas the N 1s signals of the NTP and NBM coated AuNPs give rise to a center peak position of 409.7 eV and 409.8 eV, respectively. Moreover, due to the centered distribution of the electrons on the detector, the signal shows a significant contribution from the NP beam (see Fig. S4†). Nevertheless, due to the proximity of the peaks the decomposition of the N 1s signal of NTP and NBM from the contribution of residual N_2 gas in the chamber is not precisely possible and an uncertainty remains. In XPS measurements of the NTP monolayer on an Au(111) substrate by Nielsen *et al.* and Waske *et al.*, the N 1s peak has been observed at 405.5 eV and 405.4 eV, respectively, with respect to the Fermi level and consequently the expected shift of 4.5 eV due to the AuNP work function would lead to the observed overlap.[66,67] The O 1s spectrum of NTP and NBM capped AuNPs is dominated by the O 1s signal of gaseous water at 539.9 eV,[68,69] which has been used to precisely calibrate the binding energy. The O 1s signal originating from the nitro group of the molecules is located well separated from the water peak at 537.4 eV, for NTP and NBM likewise.

The C 1s spectrum of NTP capped AuNPs has been recorded with a high kinetic energy resolution (FWHM = 0.66 eV) to distinguish the signals of the different carbon atoms (see Fig. 4(e)). According to DFT calculations of NTP on an Au_{30} cluster two main signal components can be expected with a ratio of 1 : 2 (see Fig. S7†), wherein one signal originates from the sp^2 hybridized C atoms 2, 3, 5 and 6 bound to two C and one H atom and a second signal from the C atoms 1 and 4 bound to the nitro and the thiol group, respectively, which are expected to be shifted by approximately 1 eV towards higher binding energy. This is comparable to previous interpretations of XPS measurements of NTP on an Au(111) substrate.[67] However, by taking into account the given experimental energy resolution, which has been verified by the 2s and 2p ionization edges of Ar gas, the experimental spectrum is significantly broadened compared to the theoretical predictions (see Fig. 4(e)). There are several effects that might explain the broadening of the C 1s spectrum of NTP on the surface of a nanoparticle. It was reported previously by Taucher *et al.* that in the XPS measurements of the C 1s states of molecular monolayers on gold surfaces an electrostatic environment influenced by internal dipole moments of the molecules and their intermolecular interaction must be considered in addition to the chemical environment of the C atoms.[64] Besides the effect of intramolecular surface dipoles shifting the C 1s states, it is also possible that the C 1s signal is broadened by the contributions of NTP molecules bound to surface sites with different work functions. A third possibility is a broadening due to thermal atom motion and intermolecular interactions in the NTP layer as described by Ehlert *et al.*[70] In Fig. 4(f) the C 1s spectrum of NBM on AuNPs is presented together with the calculated spectrum for NBM on an Au_{30} cluster (see Fig. S8†) taking into account the experimental resolution. Also in the case of NBM the experimental C 1s spectrum is broadened compared to the DFT calculations. The center of the C 1s peak for NBM, located at 290.0 eV, is shifted by 0.7 eV to higher BEs compared to the signal of NTP located at 289.3 eV. Hence, the shift of the C 1s signals of the two AuNP ligand systems is comparable to the shift of the Au 4f signals.

Conclusions

The Au 4f states of surface and bulk of ligand capped isolated AuNPs have been determined by PE dependent measurements, to modulate the escape depth of the photoelectrons. It has been shown that there is a significant shift of Au 4f states in the outer Au layer, which significantly depends on the adsorbed ligand molecule and might be caused by different dipole moments that modify the work function of the AuNP surface. The range of this effect is limited to the topmost atomic layer of the AuNPs. By the modification of the interface dipoles due to the functional groups of the molecules or different orientations to the surface, *e.g.* as a consequence of the packing density, the charge transfer between NPs and adsorbed molecules can be tuned. This allows for the engineering of NP systems using tightly bound ligands in plasmonic catalysis. Moreover, also the core level states of the ligands, most remarkably the C 1s states, are affected by the dipole moments or due to the binding of the molecules to different adsorption sites. These effects need to be considered by the evaluation of the XPS core level states of ligands bound to NP surfaces.

Methods

Chemicals

$AuHCl_4$, trisodium citrate (TSC), and 4-nitrobenzylmercaptan (NBM) have been purchased from Sigma Aldrich and 4-nitrothiophenol (NTP) has been purchased from Alfa Aesar. All chemicals have been used without further purification.

Preparation of AuNPs

AuNPs have been synthesized by citrate reduction of $HAuCl_4$ according to a modified version of the Turkevich protocol.[71] Briefly, a 500 mL stirred aqueous solution of 1 mM $HAuCl_4$ has been heated up in a 1 L 2 neck round bottom flask to a rolling boil under reflux in an oil bath. Subsequently, 4 mL of 500 mM TSC has been added using a syringe and the solution has been kept boiling for 20 more minutes and cooled down to room temperature and stored at 4 °C. The diameter of the AuNPs

determined from SEM images is 8.7 ± 1.7 nm and the maximum of the SPR is located at $\lambda = 518$ nm (see Fig. S1†).

In order to exchange the citrate ligands of the AuNPs with the analyte molecules, the AuNP solution has been incubated with NTP or NBM overnight. Using 15 mL Amicon filters (Merck Millipore) the AuNP solution has been centrifuged at 3000 g for 10 min and refilled with H_2O Milli Q trice. After the final centrifugation step the concentration of the AuNP solution has been adjusted to approximately 3 mM referring to the Au atoms in the solution. Raman spectra validating the bond of the ligands to the AuNP surface are shown in Fig. S2.†

Synchrotron XPS

The XPS measurements of isolated AuNPs have been performed at the PLEIADES beamline at the synchrotron SOLEIL using a multipurpose source chamber (MPSC).[72,73] The AuNPs have been brought to the gas phase from a colloidal solution using a TSI 3076 atomizer, with argon as the carrier gas at 35 Psi. The solvent (water) has been mainly removed by passing the aerosol through silica desiccators. The AuNPs then have entered the MPSC through a limiting orifice (240 μm) and have been focused with an aerodynamic lens system through a skimmer (1.5 mm) into the ionization chamber. At the entrance of the VG Scienta R4000 hemispherical electron energy analyzer the Au nanoparticle beam has been crossed with the soft X-ray photon beam produced by a permanent magnet APPLE II type undulator, with a period of 80 mm, in combination with a high-flux, 600 L mm^{-1} grating of the modified Petersen plane grating monochromator used to monochromatize the synchrotron radiation. The binding energy of the Au 4f energy level was calibrated according to the kinetic difference with respect to the 2p and 3s ionization edges of the carrier argon gas[42] at all recorded PEs (see Fig. SI 3†). The linearity of the kinetic energy scale has been validated by using 2s, 2p, 3p and 3s ionization edges[42] and KLL Auger electrons[74] of the carrier argon gas, as discussed before.[75] The overall uncertainty of BE due to the calibration is estimated to be 0.1–0.2 eV. It should be noted that in the PLEIADES setup, the photoelectron lines from the focused AuNPs can be resolved from those produced by residual H_2O solvent molecules and Ar carrier gas, which are not focused by the aerodynamic lens.[75]

The peaks have been distinguished using XPSPEAK 4.1 software assuming a Gaussian–Lorentzian fit function with a ratio of 80%. The FWHM has been fixed for all components to the experimentally determined FWHM from the measurements of the Ar ionization edges.

DFT

DFT calculations were performed with the quantum chemical package Gaussian 16.[76] The gold–molecule complexes were optimized using the global hybrid functional B3LYP.[77,78] The TZVP basis set[79] was used for the H, C, N, O, and S atoms and LANL2TZ(f) effective core potential with the corresponding basis set[80] (of triple zeta valence orbital quality and an f polarization function) was used for the Au atoms. Spin-unrestricted DFT was used for doublet species (neutral complexes with an even number of gold atoms; one gold atom) and spin-restricted DFT for singlet species (neutral complexes with a single gold atom; gold clusters with an even number of gold atoms).

Au 4f orbital shifts were calculated with the all-electron ANO-R basis set[81] (the largest one in the recent ANO-R series) for gold and TZVP for the other atoms, again employing B3LYP.

The LANL2TZ(f) and ANO-R basis sets were downloaded from the Basis Set Exchange[82] website (https://www.basissetexchange.org/). The complexes of NTP and NBM with 1, 2, 10, and 30 atoms were considered. Further details of the used models are reported in ref. 37.

Conflicts of interest

There are no conflicts to declare.

Acknowledgements

IB, RS and AM acknowledge support by the European Research Council (ERC; consolidator grant no. 772752), and we acknowledge beamtime at the synchrotron SOLEIL at the beamline PLEIADES through project 20191485.

References

1 S. Linic, P. Christopher and D. B. Ingram, *Nat. Mater.*, 2011, **10**, 911–921.
2 S. Linic, U. Aslam, C. Boerigter and M. Morabito, *Nat. Mater.*, 2015, **14**, 567–576.
3 D. C. Ratchford, *ACS Nano*, 2019, **13**, 13610–13614.
4 E. Kazuma and Y. Kim, *Angew. Chem., Int. Ed.*, 2019, **58**, 4800–4808.
5 M. J. Kale, T. Avanesian and P. Christopher, *ACS Catal.*, 2014, **4**, 116–128.
6 A. Manjavacas, J. G. Liu, V. Kulkarni and P. Nordlander, *ACS Nano*, 2014, **8**, 7630–7638.
7 G. V. Hartland, L. V. Besteiro, P. Johns and A. O. Govorov, *ACS Energy Lett.*, 2017, **2**, 1641–1653.
8 P. Christopher and M. Moskovits, *Annu. Rev. Phys. Chem.*, 2017, **68**, 379–398.
9 K. Chen and H. Wang, *Mol. Syst. Des. Eng.*, 2021, **6**, 250–280.
10 R. Schürmann and I. Bald, *Nanoscale*, 2017, **9**, 1951–1955.
11 A. Dutta, R. Schürmann, S. Kogikoski, N. S. Mueller, S. Reich and I. Bald, *ACS Catal.*, 2021, **11**, 8370–8381.
12 C.-F. Wang, B. T. O'Callahan, D. Kurouski, A. Krayev and P. Z. El-Khoury, *J. Phys. Chem. Lett.*, 2020, **11**, 3809–3814.
13 R. Schürmann, K. Ebel, C. Nicolas, A. R. Milosavljević and I. Bald, *J. Phys. Chem. Lett.*, 2019, **10**, 3153–3158.
14 N. C. Brandt, E. L. Keller and R. R. Frontiera, *J. Phys. Chem. Lett.*, 2016, **7**, 3179–3185.
15 H.-K. Choi, K. S. Lee, H.-H. Shin and Z. H. Kim, *J. Phys. Chem. Lett.*, 2016, **7**, 4099–4104.
16 H.-K. Choi, W.-H. Park, C.-G. Park, H.-H. Shin, K. S. Lee and Z. H. Kim, *J. Am. Chem. Soc.*, 2016, **138**, 4673–4684.
17 Q. Ding, M. Chen, Y. Fang, Z. Zhang and M. Sun, *J. Phys. Chem. C*, 2017, **121**, 5225–5231.

18 W. Koopman, R. M. Sarhan, F. Stete, C. N. Z. Schmitt and M. Bargheer, *Nanoscale*, 2020, **12**, 24411–24418.
19 X. Ren, E. Cao, W. Lin, Y. Song, W. Liang and J. Wang, *RSC Adv.*, 2017, **7**, 31189–31203.
20 R. M. Sarhan, W. Koopman, R. Schuetz, T. Schmid, F. Liebig, J. Koetz and M. Bargheer, *Sci. Rep.*, 2019, **9**, 3060.
21 M. Zhang, L.-B. Zhao, W.-L. Luo, R. Pang, C. Zong, J.-Z. Zhou, B. Ren, Z.-Q. Tian and D.-Y. Wu, *J. Phys. Chem. C*, 2016, **120**, 11956–11965.
22 Q. Zhang and H. Wang, *J. Phys. Chem. C*, 2018, **122**, 5686–5697.
23 Z. Zhang, T. Deckert-Gaudig, P. Singh and V. Deckert, *Chem. Commun.*, 2015, **51**, 3069–3072.
24 Z. Zhang, D. Kinzel and V. Deckert, *J. Phys. Chem. C*, 2016, **120**, 20978–20983.
25 R. Schürmann, T. F. M. Luxford, I. S. Vinklárek, J. Kočišek, M. Zawadzki and I. Bald, *J. Chem. Phys.*, 2020, **153**, 104303.
26 D. Lee and S. Yoon, *J. Phys. Chem. C*, 2020, **124**, 15879–15885.
27 C. D. Lindstrom and X.-Y. Zhu, *Chem. Rev.*, 2006, **106**, 4281–4300.
28 W. E. Ford, D. Gao, N. Knorr, R. Wirtz, F. Scholz, Z. Karipidou, K. Ogasawara, S. Rosselli, V. Rodin, G. Nelles and F. von Wrochem, *ACS Nano*, 2014, **8**, 9173–9180.
29 X. Peng, L. Hu, F. Qin, Y. Zhou and P. K. Chu, *Adv. Mater. Interfaces*, 2018, **5**, 1701404.
30 H. Häkkinen, *Nat. Chem.*, 2012, **4**, 443–455.
31 P. C. Rusu, G. Giovannetti, C. Weijtens, R. Coehoorn and G. Brocks, *J. Phys. Chem. C*, 2009, **113**, 9974–9977.
32 R. Otero, A. L. Vázquez de Parga and J. M. Gallego, *Surf. Sci. Rep.*, 2017, **72**, 105–145.
33 E. Zojer, T. C. Taucher and O. T. Hofmann, *Adv. Mater. Interfaces*, 2019, **6**, 1900581.
34 S.-Y. Hong, P.-C. Yeh, J. I. Dadap and R. M. Osgood, *ACS Nano*, 2012, **6**, 10622–10631.
35 O. T. Hofmann, D. A. Egger and E. Zojer, *Nano Lett.*, 2010, **10**, 4369–4374.
36 M. Gärtner, E. Sauter, G. Nascimbeni, A. Petritz, A. Wiesner, M. Kind, T. Abu-Husein, M. Bolte, B. Stadlober, E. Zojer, A. Terfort and M. Zharnikov, *J. Phys. Chem. C*, 2018, **122**, 28757–28774.
37 W. Koopman, E. Titov, R. M. Sarhan, T. Gaebel, R. Schürmann, A. Mostafa, S. Kogikoski, A. R. Milosavljević, F. Stete, F. Liebig, C. N. Schmitt, J. Koetz, I. Bald, P. Saalfrank and M. Bargheer, *Adv. Mater. Interfaces*, 2021, **8**, 2101344.
38 J. Liu, Z.-Y. Cai, W.-X. Sun, J.-Z. Wang, X.-R. Shen, C. Zhan, R. Devasenathipathy, J.-Z. Zhou, D.-Y. Wu, B.-W. Mao and Z.-Q. Tian, *J. Am. Chem. Soc.*, 2020, **142**, 17489–17498.
39 G. Greczynski and L. Hultman, *Prog. Mater. Sci.*, 2020, **107**, 100591.
40 M. P. Seah, I. S. Gilmore and G. Beamson, *Surf. Interface Anal.*, 1998, **26**, 642–649.
41 D. R. Baer, K. Artyushkova, H. Cohen, C. D. Easton, M. Engelhard, T. R. Gengenbach, G. Greczynski, P. Mack, D. J. Morgan and A. Roberts, *J. Vac. Sci. Technol., A*, 2020, **38**, 031204.
42 A. C. Thompson, D. T. Attwood, E. M. Gullikson, M. R. Howells, J. B. Kortright, A. L. Robinson, J. H. Underwood, K.-J. Kim, J. Kirz, I. Lindau, P. Pianetta, H. Winick, G. P. Williams and J. H. Scofield, *X-Ray Data Booklet*, Berkeley, 2009.
43 D. Cahen and A. Kahn, *Adv. Mater.*, 2003, **15**, 271–277.
44 A. Kahn, *Mater. Horiz.*, 2016, **3**, 7–10.
45 S. Axnanda, M. Scheele, E. Crumlin, B. Mao, R. Chang, S. Rani, M. Faiz, S. Wang, A. P. Alivisatos and Z. Liu, *Nano Lett.*, 2013, **13**, 6176–6182.
46 M. F. Lichterman, S. Hu, M. H. Richter, E. J. Crumlin, S. Axnanda, M. Favaro, W. Drisdell, Z. Hussain, T. Mayer, B. S. Brunschwig, N. S. Lewis, Z. Liu and H.-J. Lewerenz, *Energy Environ. Sci.*, 2015, **8**, 2409–2416.
47 J. Hwang, A. Wan and A. Kahn, *Mater. Sci. Eng., R*, 2009, **64**, 1–31.
48 J. B. Gilbert, M. F. Rubner and R. E. Cohen, *Proc. Natl. Acad. Sci. U. S. A.*, 2013, **110**, 6651–6656.
49 M. P. Seah and W. A. Dench, *Surf. Interface Anal.*, 1979, **1**, 2–11.
50 C. Passiu, A. Rossi, M. Weinert, W. Tysoe and N. D. Spencer, *Appl. Surf. Sci.*, 2020, **507**, 145084.
51 C. J. Powell and A. Jablonski, *J. Phys. Chem. Ref. Data*, 1999, **28**, 19–62.
52 H. Shinotsuka, S. Tanuma, C. J. Powell and D. R. Penn, *Surf. Interface Anal.*, 2015, **47**, 871–888.
53 C. J. Powell, *J. Vac. Sci. Technol.*, 2020, **38**, 23209.
54 M. de Anda Villa, J. Gaudin, D. Amans, F. Boudjada, J. Bozek, R. Evaristo Grisenti, E. Lamour, G. Laurens, S. Macé, C. Nicolas, I. Papagiannouli, M. Patanen, C. Prigent, E. Robert, S. Steydli, M. Trassinelli, D. Vernhet and A. Lévy, *Langmuir*, 2019, **35**, 11859–11871.
55 M. Tchaplyguine, M.-H. Mikkelä, C. Zhang, T. Andersson and O. Björneholm, *J. Phys. Chem. C*, 2015, **119**, 8937–8943.
56 F. Chesneau, J. Zhao, C. Shen, M. Buck and M. Zharnikov, *J. Phys. Chem. C*, 2010, **114**, 7112–7119.
57 M. Zharnikov, *J. Electron Spectrosc. Relat. Phenom.*, 2010, **178–179**, 380–393.
58 Y. Zhang, O. Pluchery, L. Caillard, A.-F. Lamic-Humblot, S. Casale, Y. J. Chabal and M. Salmeron, *Nano Lett.*, 2015, **15**, 51–55.
59 In*CRC handbook of chemistry and physics. A ready-reference book of chemical and physical data: 2012-2013*, ed. W. M. Haynes, D. R. Lide and T. J. Bruno, CRC Press, Boca Raton (Fla.), London, New York, 93rd edn, 2012.
60 P. H. Citrin, G. K. Wertheim and Y. Baer, *Phys. Rev. Lett.*, 1978, **41**, 1425–1428.
61 G. K. Wertheim, S. B. DiCenzo and S. E. Youngquist, *Phys. Rev. Lett.*, 1983, **51**, 2310–2313.
62 J. Radnik, C. Mohr and P. Claus, *Phys. Chem. Chem. Phys.*, 2003, **5**, 172–177.
63 D. M. Alloway, A. L. Graham, X. Yang, A. Mudalige, R. Colorado, V. H. Wysocki, J. E. Pemberton, T. R. Lee, R. J. Wysocki and N. R. Armstrong, *J. Phys. Chem. C*, 2009, **113**, 20328–20334.
64 T. C. Taucher, I. Hehn, O. T. Hofmann, M. Zharnikov and E. Zojer, *J. Phys. Chem. C*, 2016, **120**, 3428–3437.

65 F. Vitale, I. Fratoddi, C. Battocchio, E. Piscopiello, L. Tapfer, M. V. Russo, G. Polzonetti and C. Giannini, *Nanoscale Res. Lett.*, 2011, **6**, 103.
66 J. U. Nielsen, M. J. Esplandiu and D. M. Kolb, *Langmuir*, 2001, **17**, 3454–3459.
67 P. Waske, T. Wächter, A. Terfort and M. Zharnikov, *J. Phys. Chem. C*, 2014, **118**, 26049–26060.
68 R. Sankari, M. Ehara, H. Nakatsuji, Y. Senba, K. Hosokawa, H. Yoshida, A. de Fanis, Y. Tamenori, S. Aksela and K. Ueda, *Chem. Phys. Lett.*, 2003, **380**, 647–653.
69 B. Winter, E. F. Aziz, U. Hergenhahn, M. Faubel and I. V. Hertel, *J. Chem. Phys.*, 2007, **126**, 124504.
70 C. Ehlert, D. Kröner and P. Saalfrank, *J. Electron Spectrosc. Relat. Phenom.*, 2015, **199**, 38–45.
71 J. Turkevich, P. C. Stevenson and J. Hillier, *Discuss. Faraday Soc.*, 1951, **11**, 55.
72 O. Sublemontier, C. Nicolas, D. Aureau, M. Patanen, H. Kintz, X. Liu, M.-A. Gaveau, J.-L. Le Garrec, E. Robert, F.-A. Barreda, A. Etcheberry, C. Reynaud, J. B. Mitchell and C. Miron, *J. Phys. Chem. Lett.*, 2014, **5**, 3399–3403.
73 A. Lindblad, J. Söderström, C. Nicolas, E. Robert and C. Miron, *Rev. Sci. Instrum.*, 2013, **84**, 113105.
74 L. O. Werme, T. Bergmark and K. Siegbahn, *Phys. Scr.*, 1973, **8**, 149–153.
75 D. Danilović, D. K. Božanić, R. Dojčilović, N. Vukmirović, P. Sapkota, I. Vukašinović, V. Djoković, J. Bozek, C. Nicolas, S. Ptasinska and A. R. Milosavljević, *J. Phys. Chem. C*, 2020, **124**, 23930–23937.
76 M. J. Frisch, G. W. Trucks, H. B. Schlegel, G. E. Scuseria, M. A. Robb, J. R. Cheeseman, G. Scalmani, V. Barone, G. A. Petersson, H. Nakatsuji, X. Li, M. Caricato, A. V. Marenich, J. Bloino, B. G. Janesko, R. Gomperts, B. Mennucci, H. P. Hratchian, J. V. Ortiz, A. F. Izmaylov, J. L. Sonnenberg, D. Williams-Young, F. Ding, F. Lipparini, F. Egidi, J. Goings, B. Peng, A. Petrone, T. Henderson, D. Ranasinghe, V. G. Zakrzewski, J. Gao, N. Rega, G. Zheng, W. Liang, M. Hada, M. Ehara, K. Toyota, R. Fukuda, J. Hasegawa, M. Ishida, T. Nakajima, Y. Honda, O. Kitao, H. Nakai, T. Vreven, K. Throssell, J. A. Jr Montgomery, J. E. Peralta, F. Ogliaro, M. J. Bearpark, J. J. Heyd, E. N. Brothers, K. N. Kudin, V. N. Staroverov, T. A. Keith, R. Kobayashi, J. Normand, K. Raghavachari, A. P. Rendell, J. C. Burant, S. S. Iyengar, J. Tomasi, M. Cossi, J. M. Millam, M. Klene, C. Adamo, R. Cammi, J. W. Ochterski, R. L. Martin, K. Morokuma, O. Farkas, J. B. Foresman and D. J. Fox, *Gaussian 16*, Revision C.01, Gaussian, Inc., Wallingford CT, 2016.
77 P. J. Stephens, F. J. Devlin, C. F. Chabalowski and M. J. Frisch, *J. Phys. Chem.*, 1994, **98**, 11623–11627.
78 A. D. Becke, *J. Chem. Phys.*, 1993, **98**, 5648–5652.
79 A. Schäfer, C. Huber and R. Ahlrichs, *J. Chem. Phys.*, 1994, **100**, 5829–5835.
80 L. E. Roy, P. J. Hay and R. L. Martin, *J. Chem. Theory Comput.*, 2008, **4**, 1029–1031.
81 J. P. Zobel, P.-O. Widmark and V. Veryazov, *J. Chem. Theory Comput.*, 2020, **16**, 278–294.
82 B. P. Pritchard, D. Altarawy, B. Didier, T. D. Gibson and T. L. Windus, *J. Chem. Inf. Model.*, 2019, **59**, 4814–4820.